PHYSICAL REVIEW A **82**, 032114 (2010)

Double-slit vacuum polarization effects in ultraintense laser fields

B. King,[*] A. Di Piazza,[†] and C. H. Keitel[‡]
Max-Planck-Institut für Kernphysik, Saupfercheckweg 1, D-69117 Heidelberg, Germany

(Received 15 April 2010; published 17 September 2010)

The influence of the strong laser-driven vacuum on a propagating electromagnetic probe wave has been studied in detail. We investigate two scenarios, which comprise a focused probe laser beam that passes through a region of vacuum polarized by an ultraintense laser field. By splitting this strong field into two separated monochromatic Gaussian pulses that counterpropagate in a plane perpendicular to the probe-field axis, we demonstrate a leading-order light-by-light diffraction effect that generates an interference pattern reminiscent of the classic double-slit experiment. We calculate the total number of probe photons diffracted as well as the number diffracted into regions where the vacuum polarization signal is higher than the probe background. In addition, we calculate the induced ellipticity and polarization rotation in the probe beam and show how, in the realistic situation in which the centers of the two strong fields are not exactly aligned, certain ranges of beam separation and observation distance may actually lead to an increase over the idealized case of a single strong laser beam.

DOI: 10.1103/PhysRevA.82.032114 PACS number(s): 12.20.Fv, 42.50.Xa

I. INTRODUCTION

That strong electromagnetic fields can modify the dielectric properties of the quantum vacuum has been known since the pioneering work of Heisenberg and Euler [1], Weisskopf [2], and Sauter [3]. Quantum electrodynamics (QED) predicts that when the electromagnetic-field strength nears the critical Schwinger limit required to spontaneously create an electron-positron pair with an electron of charge $-e < 0$ and mass m within the reduced Compton wavelength $\lambda\!\!\!^{-}_c = \hbar/mc$, a range of nonlinear vacuum polarization effects (VPEs) should become observable. The corresponding electric field of $E_{\text{cr}} = \sqrt{4\pi} m^2c^3/\hbar e = 1.3 \times 10^{16}$ V cm^{-1} in Lorentz-Heaviside units, would certainly allow one to access *absorptive* VPE processes, namely, which involve real electron-positron pair creation, whose rates would become large enough to easily be observed. Moreover, recent calculations show that these effects, in the presence of loan fields, can already clearly be observed at intensities orders of magnitude below critical values [4–7]. Such VPE processes have also been discussed as a probe for new fundamental physics, with current limits clarified and new experiments proposed [8–12]. Since these processes are exponentially suppressed, for the case in earth-bound laboratories, where the electric fields involved are much less than E_{cr}, it is *refractive* VPE processes, which involve virtual electron-positron pairs that are most likely to be observed. Photon-photon scattering is one example of a refractive VPE [13], which has already been carried out as Delbrück scattering, which involves virtual photons in the Coulomb field of a heavy nucleus [14], where the atomic number Z is $\lesssim 1/\alpha$ and $\alpha = e^2/4\pi\hbar c \approx 1/137$ is the fine-structure constant, but has since eluded detection for purely real photons [15]. This effect could be measured by virtue of polarization-dependent emission in four-wave mixing [16] by using the transverse-electric modes of plane waves to generate a resonant coupling in a waveguide [17] or by using sufficiently intense lasers to compensate for the small cross section to induce a phase shift in lasers that pass through one another [18,19] (for a review of the applications of relativistic lasers, see Refs. [20–22]). Other nonlinear vacuum effects include photon acceleration [23], photon splitting in atomic fields [24], pair plasmas [25], and laser fields [26] as well as the corresponding reverse process of vacuum high-order harmonic generation (e.g., in various laser setups [27,28] or in a mixed Coulomb and laser-field setup [29]). The corresponding critical bound of the magnetic field $B_{\text{cr}} = \sqrt{4\pi} m^2c^3/\hbar e = 4.4 \times 10^{13}$ G can be surpassed by ultramagnetized neutron stars or “magnetars” [30] (for a review on x-ray pulsars, see Ref. [31]), which provide an inhomogeneous trigger for nonlinear effects, such as vacuum birefringence and photon ray bending [32] as well as photon splitting [33,34]. The possibility of laboratory-based experiments that measure second-harmonic generation within a constant inhomogeneous magnetic field has also been considered [35]. The current PVLAS (polarizzazione del vuoto con laser) experiment uses a slowly varying magnetic field to attempt to detect refractive-regime vacuum-induced birefringence and dichroism through rotation in the polarization of a probe laser wave [36]. In addition to in a magnetic field, birefringence can also be induced in the vacuum by, for example, a laser field in this regime [37–40]. This latter scenario, and that of vacuum-induced diffraction are two examples of refractive VPEs that we further develop in the current paper.

At the time of writing, the record for the highest intensity laser ever produced is held by the HERCULES laser, and stands at 2×10^{22} W cm^{-2} [41], seven orders of magnitude removed from the Schwinger limit intensity of $I_{\text{cr}} = cE_{\text{cr}}^2/2 = 2.3 \times 10^{29}$ W cm^{-2}. We foresee that with the next generation of lasers currently being built, we will soon be in a much better position to test vacuum effects and so work with the quoted values for intended intensity and photon energy ranges in the coming decade. Examples of strong-field lasers are the ELI (extreme light infrastructure) and the HiPER (high power laser energy research) facilities with target intensity values of 10^{26} W cm^{-2} [42,43]. The petawatt field synthesizer [44],

---

[*] ben.king@mpi-hd.mpg.de
[†] dipiazza@mpi-hd.mpg.de
[‡] keitel@mpi-hd.mpg.de

while planning a lower intensity of 10^{22} W cm^{-2}, will have a repetition rate of 10 Hz, which could be more favorable in certain situations and provides an example of a cutting-edge system to be commissioned in the near future. Free-electron lasers (FELs), where undulating electrons provide the lase medium, such as the x-ray free-electron laser (XFEL) and the linac coherent light source (LCLS) could also be used to polarize the quantum vacuum, especially with the so-called “goal” parameters quoted in Ref. [45]. However, a further application of the FELs, one that could be reached sooner, would be as probe-field lasers, whose alteration, when passing through vacuum polarized regions, could be measured. The XFEL and the LCLS would be ideal for measuring refractive effects, which are, in general, proportional to laser frequency, as they allow continuous adjustment of the probe wavelength down to a minimum of 0.1 and 0.15 nm, respectively [46,47].

This paper concerns itself with laser-induced vacuum polarization effects in the spirit of Ref. [40]. Here, the change in polarization and ellipticity of a planar Gaussian probe field that passes through a region of the vacuum polarized by a perpendicular standing wave formed by two counterpropagating ultraintense ($I_0 \geqslant 10^{23}$ W cm^{-2}) Gaussian beams, was calculated up until the point where probe defocusing becomes important. We compare and expand upon this simple setup with the following enhancements (see Fig. 1):

(i) The two counterpropagating strong-field wave triggers for VPEs are separated in the plane perpendicular to their propagation, thereby modelling a more realistic situation. This makes sense, first, from an experimental point of view, to know how VPEs are sensitive to laser alignment, and, second, allows us to derive an interference effect as different parts of the probe beam pass through the double-slit-like vacuum-polarized region. This will even turn out to increase probe-beam polarization rotation and ellipticity.

(ii) Defocusing terms were introduced into the probe beam and the vacuum-induced ellipticity and rotation of the probe polarization were correspondingly updated. This extends the limited range of detector distances in Ref. [40], where we could have compared theory to experiment, as our new expressions are also valid in the far-field diffraction zone, where they converge to a nonzero value.

(iii) The electric field generated in the new setup by the current of the polarized vacuum, which we, henceforth, label the diffracted field, was also calculated in the probe beam's transverse plane, which allows us to again model the more realistic situation where a detector is placed off axis, in regions where the diffracted field, which has a wider spread, is larger than the probe background.

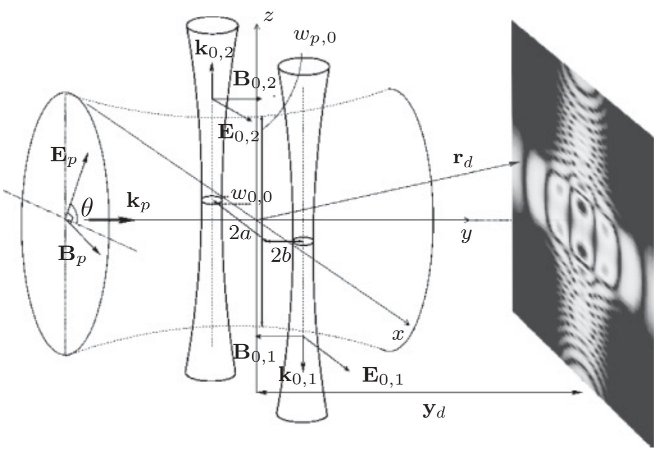

FIG. 1. The double-slit experimental setup. A monochromatic Gaussian probe beam with electric- and magnetic-field vectors $\mathbf{E}_p$ and $\mathbf{B}_p$, respectively, wave vector $\mathbf{k}_p$, linearly polarized at an angle θ to the x axis in the x-z plane and with a waist $w_{p,0}$, much greater than the strong-field beam waist $w_{0,0}$ impinges on and is perpendicular to two parallel counterpropagating monochromatic and Gaussian strong-field waves with amplitudes $E_0/\sqrt{2} \gg E_p$, electric and magnetic fields in the x-y plane $\mathbf{E}_{0,1}, \mathbf{E}_{0,2}$ and $\mathbf{B}_{0,1}, \mathbf{B}_{0,2}$, respectively, wave vectors $\pm\mathbf{k}_0 = (0,0,\mp\omega_0)$, $\omega_0 \ll \omega_p$, with foci at $(x,y) = (a,b)$ and $(x,y) = (-a,-b)$. The results of this process are then measured a distance r_d from the center of the interaction region.

Throughout, we will make the analogy with the single- and double-slit diffraction experiment. According to Babinet's principle, the diffraction pattern generated by light that passes an opaque obstacle is the same as that for light that traverses an aperture with the same shape as the obstacle [48]. Regions of the vacuum polarized by the two strong-field laser beams then represent translucent obstacles for photons in the probe beam, by having, as we will show, a nontrivial polarization and magnetization. Unlike the typically sharp two-dimensional slits used in demonstration experiments, the strong lasers, which are Gaussian in beam profile, form smooth, three-dimensional slits. One consequence of this will be that no single-slit fringes occur in the far field. However, the probe photons scattered from each strong beam will interfere with one another, and, in this way, we *will* have a double slit. As the scattering of probe photons occurs with such a small probability, the complete double-slit pattern will only be observable when the background of probe photons that pass unperturbed through the apparatus, is subtracted. At the detector, the total field will, in general, consist of the probe signal plus the vacuum contribution of the scattered photons. In calculating the interference between these two fields, we demonstrate an additional diffractive effect of the polarized vacuum, which we accentuate by forming the double-slit-like experimental setup. In addition, we also compare polarization results with a second beam geometry, namely, that of the probe, which propagates antiparallel to the strong field, which we label the double-shaft (or single-shaft) setup. Our results are complementary to findings in Ref. [37], which focus on only the pure diffracted intensity for a different laser geometry.

The paper is organized as follows: In Sec. II, we first introduce the Euler-Heisenberg theory upon which the results are based and the range of experimental scenarios we considered; then, in Sec. III, follows an analysis of the first part of the results, the intensity of the bare-diffracted field and the time-averaged difference in the probe plus diffracted signal in terms of the number of photons; the second part of the results deals with the change in rotation and ellipticity of polarization for both of the two geometries, and the paper is concluded with a recapitulation of the main results.

II. THEORETICAL BASIS

A. Leading-order vacuum current

By making two basic assumptions, we can drastically simplify the interaction terms that occur in our field theory [49]. From the assumption that the photon energies involved are much lower than the electron rest energy, it follows that the loop contribution of spatiotemporal extent can be consistently regarded as a single local interaction point, thereby allowing us to write down the so-called Euler-Heisenberg local point Lagrangian density $\mathcal{L}$, which we will use to describe vacuum polarization effects. Second, from the aforementioned laser intensities that are either currently available or scheduled for the future, we will work with the comfortable assumption that field strengths are much lower than critical values. Then, this allows us to use the weak-field expansion of the Euler-Heisenberg Lagrangian, the leading order of which (in a system of units adopted henceforth, $\hbar = c = 1$) reads

$$\mathcal{L} = \frac{1}{2}(E^2 - B^2) + \frac{2\alpha^2}{45m^4}[(E^2 - B^2)^2 + 7(\mathbf{E}\cdot\mathbf{B})^2], \quad (1)$$

for electric and magnetic fields $\mathbf{E}$ and $\mathbf{B}$ and their square moduli $E^2 = \mathbf{E}\cdot\mathbf{E}$, $B^2 = \mathbf{B}\cdot\mathbf{B}$, respectively. By extremizing the action with respect to the vector potential that corresponds to these fields, we achieve the following wave equations of motion, for an induced *vacuum current* $\mathbf{J}_{\text{vac}}$:

$$\nabla^2\mathbf{E} - \partial_t^2\mathbf{E} = \mathbf{J}_{\text{vac}} = \nabla \wedge \partial_t\mathbf{M} - \nabla(\nabla\cdot\mathbf{P}) + \partial_t^2\mathbf{P}, \quad (2)$$

$$\mathbf{P} := \frac{4\alpha^2}{45m^4}[2(E^2 - B^2)\mathbf{E} + 7(\mathbf{E}\cdot\mathbf{B})\mathbf{B}], \quad (3)$$

$$\mathbf{M} := -\frac{4\alpha^2}{45m^4}[2(E^2 - B^2)\mathbf{B} - 7(\mathbf{E}\cdot\mathbf{B})\mathbf{E}]. \quad (4)$$

There are many similarities one can draw between birefringent solid-state materials and the behavior of the vacuum under intense electromagnetic fields. Direct from the preceding wave equation, Eq. (2), we can liken the vacuum current to one, which represents the response from such a birefringent material, that is to say, to label $\mathbf{P}$ its polarization, and $\mathbf{M}$ its magnetization.[1] As these are functions of both $\mathbf{E}$ and $\mathbf{B}$, the inhomogeneity in our fields, which plays a central role here, is included at this point.

B. Definition of experimental scenario

In this paper, we will focus mainly on the double-slit setup sketched in Fig. 1, and will include only a summary of the polarization results for the single-shaft setup that corresponds to a head-on probe and a strong-field collision toward the end of the paper (here, we use the label shaft contrary to the one in Ref. [37], where it was also labeled a slit). For our double-slit setup, two tightly focused [we assume the diffraction limit has been reached (i.e., focused down to a wavelength)] counterpropagating monochromatic strong-field Gaussian pulses that polarize the vacuum, with waists $w_{0,0}$ centered at $(x,y) = (a,b)$ and $(x,y) = (-a,-b)$, electric fields $\mathbf{E}_{0,1}(x,y,z,t)$, $\mathbf{E}_{0,2}(x,y,z,t)$, and wave vectors $\mathbf{k}_0 = (0,0,-\omega_0)$ and $-\mathbf{k}_0 = (0,0,\omega_0)$, respectively, are permeated simultaneously by a broader and weaker linearly polarized transverse monochromatic Gaussian probe field, polarized at an angle θ to the x axis with waist $w_{p,0}$, electric field $\mathbf{E}_p$, and wave vector $\mathbf{k}_p = (0,\omega_p,0)$, which will gain a diffracted component, whose intensity and polarization will be measured some distance r_d away. By using the Gaussian beam solution from Ref. [20], in the effective interaction region, we therefore have the following:

$$\mathbf{E}_0(x,y,z,t) := [E_{0,1}(x,y,z,t) + E_{0,2}(x,y,z,t)]\hat{\mathbf{x}},$$

$$\begin{aligned} E_{0,1}(x,y,z,t) := {}& E_{0,0}(x-a,y-b,z)\sin\bigg(\psi_0 + \omega_0 t + \omega_0 z \\ &- \phi_{g,0}(z) + \frac{\omega_0 z}{2}\frac{(x-a)^2 + (y-b)^2}{z^2 + z_{r,0}^2}\bigg), \\ E_{0,2}(x,y,z,t) := {}& E_{0,0}(x+a,y+b,z)\sin\bigg(\psi_0 + \omega_0 t - \omega_0 z \\ &+ \phi_{g,0}(z) - \frac{\omega_0 z}{2}\frac{(x+a)^2 + (y+b)^2}{z^2 + z_{r,0}^2}\bigg), \end{aligned} \quad (5)$$

$$\begin{aligned} \mathbf{E}_p(x,y,z,t) := {}& E_{p,0}(x,y,z)\sin\bigg(\psi_p + \omega_p t - \omega_p y + \phi_{g,p}(y) \\ &- \frac{\omega_p y}{2}\frac{x^2 + z^2}{y^2 + y_{r,p}^2}\bigg)(\hat{\mathbf{x}}\cos\theta + \hat{\mathbf{z}}\sin\theta), \end{aligned} \quad (6)$$

where we have defined the strong- and probe-field amplitudes $E_{0,0}(x,y,z)$, $E_{p,0}(x,y,z)$, respectively, with their maximum values $E_0/\sqrt{2}$ and $E_p \ll E_0$, as

$$E_{0,0}(x,y,z) := \frac{E_0}{\sqrt{2}}\frac{e^{-(x^2+y^2)/w_0^2}}{\sqrt{1 + (z/z_{r,0})^2}},$$

$$E_{p,0}(x,y,z) := E_p\frac{e^{-(x^2+z^2)/w_p^2}}{\sqrt{1 + (y/y_{r,p})^2}}.$$

The square of the waist of focusing is defined from beam parameters as $w_0^2 := w_{0,0}^2[1 + (z/z_{r,0})^2]$, $w_p^2 := w_{p,0}^2[1 + (y/y_{r,p})^2]$, where $w_{p,0} \gg w_{0,0}$, with Rayleigh lengths defined in the usual way $z_{r,0} = \omega_0 w_{0,0}^2/2 = \pi w_{0,0}$ (as we have assumed $w_{0,0} = \lambda_0$), $y_{r,p} = \omega_p w_{p,0}^2/2$, and the Gouy phases, respectively, $\phi_{g,0}(z) = \tan^{-1}(z/z_{r,0})$, $\phi_{g,p}(y) = \tan^{-1}(y/y_{r,p})$. The fields in Eq. (5) are chosen as a first-order approximation to the solution of Maxwell's equations in vacuum (see, e.g., Ref. [20], pp. 64–65 for details on the higher-order terms in this expansion), which is an expansion in the small parameters $\epsilon_z = w_{0,0}/z_{r,0} = \lambda_0/(\pi w_{0,0}) \approx 1/\pi$ and $\epsilon_y = w_{p,0}/y_{r,p} = \lambda_p/(\pi w_{p,0}) \ll 1$ (as by definition, the probe is not intensely focused and so $w_{p,0} \gg \lambda_p$). Therefore, throughout this calculation, we work to the accuracy given by the largest term neglected in the expansion ϵ_z.

---

[1] Due to a printing error on p. 2 of Ref. [40], the magnetization appears here first with the correct overall minus sign.

The magnetic fields consistent with this level of approximation are then:

$$\mathbf{B}_0(x,y,z,t) = -[E_{0,1}(x,y,z,t) - E_{0,2}(x,y,z,t)]\hat{\mathbf{y}}, \tag{7}$$

$$\begin{aligned}\mathbf{B}_p(x,y,z,t) &= E_{p,0}(x,y,z)(\hat{\mathbf{x}}\sin\theta - \hat{\mathbf{z}}\cos\theta)\\ &\quad\times\sin\left(\psi_p + \omega_p t - \omega_p y + \phi_{g,p}(y)\right.\\ &\quad\left.-\frac{\omega_p y}{2}\frac{x^2+z^2}{y^2+y_{r,p}^2}\right).\end{aligned} \tag{8}$$

Since the probe field's strength is much lower than that of the strong field, we regard terms $\propto E_p^2, B_p^2$ and smaller as negligible in Eqs. (3) and (4). In addition, as we are only interested in the effects on the probe field, we drop terms that only depend on the strong field $\propto E_0^3, B_0^3$. With $\mathbf{E} = \mathbf{E}_0 + \mathbf{E}_p$ and $\mathbf{B} = \mathbf{B}_0 + \mathbf{B}_p$, the vacuum polarization and magnetization then become

$$\begin{aligned}\mathbf{P} = \frac{4\alpha^2}{45m^4}&[2(\mathbf{E}_0\cdot\mathbf{E}_0 - \mathbf{B}_0\cdot\mathbf{B}_0)\mathbf{E}_p\\ &+4(\mathbf{E}_0\cdot\mathbf{E}_p)\mathbf{E}_0 + 7(\mathbf{E}_0\cdot\mathbf{B}_p)\mathbf{B}_0],\end{aligned} \tag{9}$$

$$\begin{aligned}\mathbf{M} = -\frac{4\alpha^2}{45m^4}&[2(\mathbf{E}_0\cdot\mathbf{E}_0 - \mathbf{B}_0\cdot\mathbf{B}_0)\mathbf{B}_p\\ &+4(\mathbf{E}_0\cdot\mathbf{E}_p)\mathbf{B}_0 - 7(\mathbf{E}_0\cdot\mathbf{B}_p)\mathbf{E}_0].\end{aligned} \tag{10}$$

C. Diffracted field off axis

We will focus on the diffracted electric field $\mathbf{E}_d(\mathbf{r}_d,t)$ generated by the polarized vacuum current in Eq. (2), at a displacement $\mathbf{r}_d$, from the center of the interaction volume (centered at the origin of the coordinate system), in the direction of the propagation of the probe beam. By using Green's functions to solve the inhomogeneous wave equation driven by a current $\mathbf{J}(\mathbf{r},t)$, we have, in general, $\mathbf{E}_d(\mathbf{r}_d,t) = -1/(4\pi)\int d^3r|\mathbf{r}_d - \mathbf{r}|^{-1}\mathbf{J}(\mathbf{r},t-|\mathbf{r}_d-\mathbf{r}|)$ [50]. It can be seen from the definition of our current in Eq. (2) that we are going to have cubic terms in the electromagnetic field, which means cross terms between our probe and strong fields in the interaction region. As our waves are monochromatic, we see that photons of discrete energies ω_p and $\omega_p \pm 2\omega_0$, etc. will be produced. Photons with the latter energies are evanescent and can therefore be neglected, which turns out to be equivalent to averaging the expression in time. We Fourier transform our current in time in order to use this discreteness and then, as we are only interested in effects in the probe, will later set the frequency ω to ω_p:

$$\begin{aligned}\mathbf{E}_d(\mathbf{r}_d,\omega) = -\frac{1}{4\pi}\int d^3r\,dt\big[\nabla\wedge\partial_t\mathbf{M} - \nabla(\nabla\cdot\mathbf{P}) + \partial_t^2\mathbf{P}\big]\\ \times\frac{\exp[-i\omega(|\mathbf{r}_d-\mathbf{r}|+t)]}{|\mathbf{r}_d-\mathbf{r}|}.\end{aligned} \tag{11}$$

It will be useful to expand the exponential by using the assumption that the detector is placed much further away than the dimensions of the interaction volume, taken as the standard deviation width of the beams. By using $w_{0,0} < w_{p,0} \ll r_d$, and then, by assuming $(w_{0,0}/\lambda_p)(w_{p,0}/r_d)^2$, $(w_{p,0}/\lambda_p)(w_{p,0}/r_d)^3 \ll 1$, we can curtail the expansion to

$$\begin{aligned}&\frac{\exp[-i\omega(|\mathbf{r}_d-\mathbf{r}|+t)]}{|\mathbf{r}_d-\mathbf{r}|}\\ &\quad\approx\frac{1}{r_d}\exp\left\{-i\omega\left[\left(r_d - \hat{\mathbf{r}}_d\cdot\mathbf{r} + \frac{1}{2r_d}|\hat{\mathbf{r}}_d\wedge\mathbf{r}|^2\right)+t\right]\right\}.\end{aligned} \tag{12}$$

By retaining the quadratic coordinate terms, we indicate that we will be working in the Fresnel regime. We can then split Eq. (11) into three integrals and integrate by parts to remove surface terms, which we assume, by using Gaussian expressions, tend to zero at the boundaries. This leaves us with

$$\begin{aligned}\mathbf{E}_d(\mathbf{r}_d,\omega) \approx{}& \frac{\omega^2\exp[-i\omega r_d]}{4\pi r_d}\\ &\times\int d^3r\,dt(\mathbf{M}\wedge\hat{\mathbf{r}}_d + \mathbf{P} - \mathbf{P}\cdot\hat{\mathbf{r}}_d\ \hat{\mathbf{r}}_d)\\ &\times\exp\left[i\omega\left(\hat{\mathbf{r}}_d\cdot\mathbf{r} - \frac{1}{2r_d}|\hat{\mathbf{r}}_d\wedge\mathbf{r}|^2 - t\right)\right].\end{aligned} \tag{13}$$

We expect the main vectorial contribution to the probe from the vacuum polarization and magnetization to be in the x and z directions (i.e., the directions of the probe and strong electromagnetic fields). When we substitute our particular scenario by using Eqs. (9) and (10) into the previous equation and then Fourier transform back into $(\mathbf{r}_d,t)$ coordinates, we achieve the following:

$$\begin{aligned}\mathbf{E}_d(\mathbf{r}_d,t) ={}& \mathbf{E}_d^*(\mathbf{r}_d)\frac{\exp[i(-\omega_p r_d + \omega_p t + \psi_p)]}{2i}\\ &-\mathbf{E}_d(\mathbf{r}_d)\frac{\exp[-i(-\omega_p r_d + \omega_p t + \psi_p)]}{2i},\\ \mathbf{E}_d(\mathbf{r}_d) :={}& \frac{I_0}{I_{\text{cr}}}\frac{\alpha E_p}{45\lambda_p^2 r_d}\Bigg[(\mathcal{V}_1+\mathcal{V}_2)\,\mathbf{u}_1 + (\mathcal{V}_3-\mathcal{V}_4)\,\mathbf{u}_2\\ &+\left(\sum_{i=1}^{4}\mathcal{V}_i\right)\mathbf{u}_3\Bigg],\end{aligned} \tag{14}$$

where the volumes $\mathcal{V}_k$ and the vectors $\mathbf{u}_i$ are defined as the following:

$$\begin{aligned}\mathcal{V}_k :={}& \int_{-\infty}^{\infty}d^3r\exp\left[+i\omega_p\left(\frac{x^2+y^2+z^2}{2r_d} - \frac{xx_d+yy_d+zz_d}{r_d}\right.\right.\\ &\left.\left.-\frac{(xx_d+yy_d+zz_d)^2}{2r_d^3}+y\right) - \frac{x^2+z^2}{w_{p,0}^2}\right]\frac{\mathcal{I}_k}{1+(z/z_r)^2},\end{aligned} \tag{15}$$

$$\begin{aligned}\mathcal{I}_1 :={}& \exp\left(-\frac{2}{w_0^2}(x^2+y^2+a^2+b^2)\right)\exp\left[-2i\left(\omega_0 z - \phi_{g,0}(z)\right.\right.\\ &\left.\left.+\frac{\omega_0 z(x^2+y^2+a^2+b^2)}{2(z^2+z_r^2)}\right)\right],\\ \mathcal{I}_2 :={}& \exp\left(-\frac{2}{w_0^2}(x^2+y^2+a^2+b^2)\right)\exp\left[2i\left(\omega_0 z - \phi_{g,0}(z)\right.\right.\\ &\left.\left.+\frac{\omega_0 z(x^2+y^2+a^2+b^2)}{2(z^2+z_r^2)}\right)\right],\end{aligned}$$

$$\mathcal{I}_3 := \exp\left(-\frac{2}{w_0^2}[(x-a)^2+(y-b)^2]\right),$$

$$\mathcal{I}_4 := \exp\left(-\frac{2}{w_0^2}[(x+a)^2+(y+b)^2]\right);$$

$$\mathbf{u}_1 := \begin{bmatrix} \left(1-\frac{y_d}{r_d}\right)\cos\theta - \frac{x_d}{r_d}\left(\frac{x_d}{r_d}\cos\theta + \frac{z_d}{r_d}\sin\theta\right) \\ \frac{z_d}{r_d}\sin\theta + \frac{x_d}{r_d}\cos\theta - \frac{y_d}{r_d}\left(\frac{x_d}{r_d}\cos\theta + \frac{z_d}{r_d}\sin\theta\right) \\ \left(1-\frac{y_d}{r_d}\right)\sin\theta - \frac{z_d}{r_d}\left(\frac{x_d}{r_d}\cos\theta + \frac{z_d}{r_d}\sin\theta\right) \end{bmatrix},$$

$$\mathbf{u}_2 := \begin{bmatrix} \frac{z_d}{r_d}\cos\theta + \frac{7}{4}\frac{x_d}{r_d}\frac{y_d}{r_d}\sin\theta \\ \frac{7}{4}\left[\left(\frac{y_d}{r_d}\right)^2 - 1\right]\sin\theta \\ -\frac{x_d}{r_d}\cos\theta + \frac{7}{4}\frac{y_d}{r_d}\frac{z_d}{r_d}\sin\theta \end{bmatrix},$$

$$\mathbf{u}_3 := \begin{bmatrix} \left[1-\left(\frac{x_d}{r_d}\right)^2\right]\cos\theta \\ -\frac{7}{4}\frac{z_d}{r_d}\sin\theta - \frac{x_d}{r_d}\frac{y_d}{r_d}\cos\theta \\ \frac{7}{4}\frac{y_d}{r_d}\sin\theta - \frac{x_d}{r_d}\frac{z_d}{r_d}\cos\theta \end{bmatrix}.$$

The main contribution from the integrals $\mathcal{V}_i$ will be within the widths of our laser beams, and so we can regard $x,y \lesssim w_{0,0}$, $z \lesssim w_{p,0}$. If we evaluate the expression at these values, the probe-amplitude defocusing terms become $[1+(y/y_{r,p})^2]^{-1/2} \approx 1-(1/2)(y/y_{r,p})^2$, and we see that the correction $(1/2)(y/y_{r,p})^2 \ll \epsilon_z$ (the accuracy of our computation) is therefore negligible. Moreover, by considering the defocusing phase terms, when we assume these ranges for x,y, and z throughout the integration $\phi_{g,p}(y) \approx (y/y_r) \ll 1$, the final defocusing term $\omega_p y(x^2+z^2)/[2(y^2+y_{r,p}^2)] \approx 2\lambda_p w_{0,0}/(\pi w_{p,0}^2) \ll 1$ for the realistic parameters that we take for our lasers, (defined later in Sec. III). Therefore, to be consistent with our beam expansion, we have considered all probe defocusing terms as constant $[w_p(y) \to w_{p,0}]$ within the integral preceding Eq. (14). Whenever the probe occurs explicitly in expressions outside the integrals, the full space dependence will be used.

From this integral Eq. (15), it can be seen that the x and y coordinates can be integrated out to give just an integral in z [see Eq. (A1) in the Appendix]. On inspection, we notice certain factors in the complex exponential of the integrand constrain the diffracted field to be sharply peaked around $x_d \approx 0$ and $y_d \approx r_d$, which agrees with physical intuition. By taking the limits $\mathbf{r}_d \to \mathbf{y}_d \equiv (0,y_d,0)$; $a,b \to 0$, we can easily recover the expression for an on-axis measurement of a single strong beam plus probe collision given in Ref. [40]. Similarly, we can derive the diffracted magnetic field $\mathbf{B}_d(\mathbf{r}_d,\omega_p)$, and by using Maxwell's inhomogeneous equations again, show $\mathbf{B}_d(\mathbf{r}_d,\omega_p) = \hat{\mathbf{k}}_p \wedge \mathbf{E}_d(\mathbf{r}_d,\omega_p)$ to within our calculational accuracy and therefore, that the flow of energy described by Poynting's vector proceeds as $\mathbf{S}_d(\mathbf{r}_d,\omega_p) = \mathbf{E}_d(\mathbf{r}_d,\omega_p) \wedge \mathbf{B}_d(\mathbf{r}_d,\omega_p)/2 = |\mathbf{E}_d(\mathbf{r}_d,\omega_p)|^2\hat{\mathbf{k}}_p/2$, which simplifies our calculation of the intensity pattern. We have assumed our earlier conditions on $w_{0,0}$ and $w_{p,0}$ that we used in Eq. (12) as well as that of $(y_d/r_d)^2 \approx 1$. One can question how sensitive these results are to being able to align the strong-field lasers parallel to one another, by considering them to be focused from a distance away by two large mirrors. For a small rotation $\delta\phi$ of $\mathbf{k}_{0,1}$ and $\mathbf{k}_{0,2}$ around the x axis in the directions $\pm\hat{\mathbf{y}}$, respectively, one can show, for $\mathbf{B}'_{0,1} = \mathbf{B}_{0,1}\cos\delta\phi + E_{0,1}\sin\delta\phi\hat{\mathbf{z}}$, $\mathbf{B}'_{0,2} = \mathbf{B}_{0,2}\cos\delta\phi - E_{0,2}\sin\delta\phi\hat{z}$ ($\mathbf{E}'_{0,1} = \mathbf{E}_{0,1}, \mathbf{E}'_{0,2} = \mathbf{E}_{0,2}$):

$$\mathbf{P}(\delta\phi) = \mathbf{P} - \delta\phi\frac{28\alpha^2}{45m^4}\left(E_{0,1}^2 - E_{0,2}^2\right)\cos\theta\hat{\mathbf{y}} + O[(\delta\phi)^2], \tag{16}$$

$$\mathbf{M}(\delta\phi) = \mathbf{M} + \delta\phi\frac{16\alpha^2}{45m^4}\left(E_{0,1}^2 - E_{0,2}^2\right)\cos\theta\hat{\mathbf{y}} + O[(\delta\phi)^2]. \tag{17}$$

In keeping within the aforementioned bounds in the detector plane, the corrections in $\delta\phi$ cancel in the combination $(\mathbf{M} \wedge \hat{\mathbf{r}}_d + \mathbf{P} - \mathbf{P}\cdot\hat{\mathbf{r}}_d\,\hat{\mathbf{r}}_d)$, which means corrections to $\mathbf{E}_d \sim (\delta\phi)^2$, which implies, by envisaging $\delta\phi \sim 0.1$, that the parallel idealization is sufficient to within the accuracy of the present treatment $1/\pi$.

A further consideration would be what role the finite length of the strong-field beams plays during the passage of the probe beam. Both the diffracted intensity and the polarization effects that we will study are proportional to the intensity of the strong field, so the corresponding longitudinal distribution is $\sim 1/[1+(z/z_{r,0})^2]$. In the absence of a well-defined decay length, we take the effective length to be that at which the intensity falls to below $\frac{1}{10}$ of its initial value, which gives an effective length of $l_0 = 3z_{r,0} = 7.5\ \mu$m. A finite pulse length leads to consideration of the temporal envelope. For the case of a Gaussian beam, the leading temporal correction should be of the order $1/\omega_0\tau_0$, which we have already specified through our assumption of monochromaticity, to be $\ll 1$. If we ensure that the strong-field pulse length τ_0 is such that $c\tau_0 > 2l_0$, then the deviation should be negligible to within our level of accuracy (for the sake of clarity, we have temporarily reintroduced c as the speed of light in vacuum). Therefore, we choose $c\tau_0 \approx 2\times 2l_0$, with $\tau_0 = 100$ fs, which will limit the maximum strong-field intensity that obeys $I_0\tau_0 A = \mathcal{E}$ for a fixed laser energy $\mathcal{E}$ and focus area A.

III. ANALYSIS OF THE RESULTS

We present results that follow from the numerical evaluation in MATLAB of the one-dimensional integral for $\mathbf{E}_d(\mathbf{r}_d)$ given in Eq. (A1) in the Appendix.

The results are presented in two sections for (i) intensity and (ii) polarization. These are further divided into the form of intensity along the x axis, along the z axis, and in the x-z plane, followed by an explanation of the polarization rotation and ellipticity expressions along the probe propagation axis.

A. Intensity measurements off axis

The nonlinearity of the vacuum brought about by the two strong-field waves generates the diffraction patterns one would expect from a refractive solid-state material. The integral expression of $\mathbf{E}_d(\mathbf{r}_d,\omega)$ in Eq. (13) allows one to interpret the effect at hand as an example of Fresnel diffraction, by including as it does, squared coordinate terms in the exponential. By satisfying the inequality: $(w_{0,0}z_{r,0}/\lambda_p r_d)(x_d^2+z_d^2)/r_d^2 \ll 1$, we can neglect the xz cross terms in the exponential and form two independent diffraction parameters $\xi_x = w_{0,0}^2/\lambda_p r_d$ and

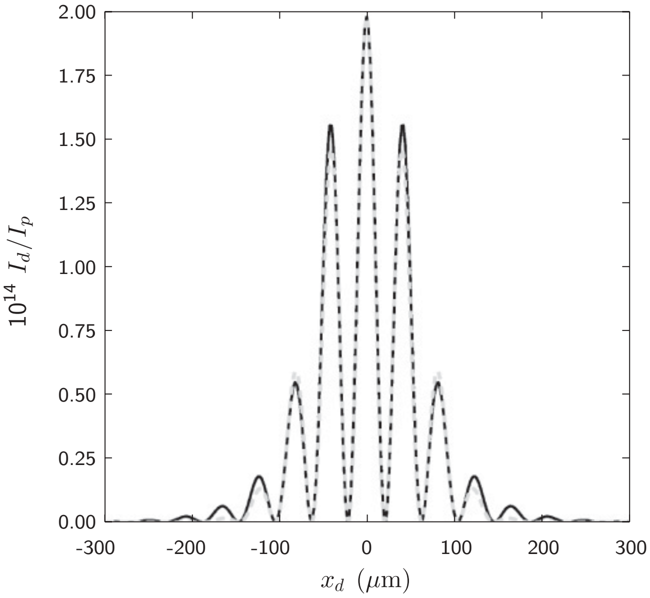

FIG. 2. The one-dimensional diffracted field along the x axis that is predicted by first-order QED theory for the parameters $a/w_{0,0} = 6$, $b/w_{0,0} = 0$, $w_{0,0} = \lambda_0 = 0.8\ \mu$m, $\lambda_p = 0.4$ nm, $w_{p,0} = 100\ \mu$m, $\theta = \pi/2$, $y_d = 1$ m, and $I_0 = 10^{24}$ W cm^{-2}, is plotted with a solid line. The dashed line indicates the result obtained by using the simplified analytical approach based on Eq. (20).

$\xi_z = w_{p,0}^2/\lambda_p r_d$, for which $\xi_{x,z} \gg 1$ implies we can take the near-field limit, while $\xi_{x,z} \ll 1$ implies we can take the far-field limit and, hence, the Fourier transform of the transmission function [48].

1. Analysis of field diffracted onto the x axis

Numerical evaluation of the leading-order QED contributions to the field diffracted onto the x axis is shown in Fig. 2. For our probe beam, we take the XFEL at DESY in Hamburg, for which we have 80 GW in a 100 fs pulse of 0.4-nm wavelength radiation focused into a waist $w_{p,0} = 100\ \mu$m [46]. We maximize the intensity of the diffracted field by setting $\theta = \pi/2$. In addition, we take, for our strong-field beams, parameters from the upcoming ELI and HiPER facilities (i.e., $\lambda_0 = 0.8\ \mu$m) and assume that they can be focused up to the diffraction limit (i.e., that $\lambda_0 = w_{0,0}$) (although the consequences of focusing to a width of a few wavelengths are not drastic for the results). As already discussed, we then choose a pulse duration of $\tau_0 = 100$ fs and a total peak intensity of $I_0 = 10^{24}$ W cm^{-2}. The strong beams are separated by $a/w_{0,0} = 6$ and observations are made at $y_d = 1$ m. In Fig. 2, we plot the diffracted field intensity, which clearly shows a familiar squared cosine, with a symmetric decaying envelope function, similar to the square of the Fourier transform of a double-slit transmission aperture. This result is expected if one notes that, with the preceding numerical parameters, the diffraction parameter ξ_x along the x direction is much smaller than unity. We also note at this point, that separation of the strong beams in the direction transverse to the detector plate has, in general, no observable effect on our numerical results for intensity, which can be understood intuitively. As the vacuum signal $\mathbf{E}_d$ is created in phase with the probe, the total phase difference between sources of vacuum waves separated by $2b$ in the longitudinal direction is $2b\omega_p(1 - y_d/r_d)$, as can be seen from Eq. (12) in the far field. By setting $z_d = 0$ for simplicity, the condition to be fulfilled for a corresponding first minimum would be $\lambda_p/2 = b(x_d/r_d)^2$. Since we are using an x-ray probe, for realistic separation of the strong-field beams of the order of a few multiples of $w_{0,0}$, the first minimum would occur for values of x_d far outside our detector plate. Moreover, for a finite strong-beam x separation $2a$, any additional separation of the beams in the y direction, will not create an appreciable separation perpendicular to the diffracted wave vector. For these reasons, we can disregard b and set it equal to zero in this section.

In the present case, $x_d, z_d \ll y_d$, and this implies that the terms proportional to the vectors $\mathbf{u}_1$ and $\mathbf{u}_2$ in $\mathbf{E}_d(\mathbf{r}_d)$ are negligible. Also, we notice that for the typical situation $w_{0,0} + a \ll w_{p,0}$, the cosine term formed from the integrals $\mathcal{V}_1 + \mathcal{V}_2$ can be neglected when both:

$$\frac{2\pi w_{p,0}}{\lambda_0} \gg \sqrt[4]{1+\left(\frac{\pi w_{p,0}^2}{y_d\lambda_p}\right)^2} \quad \text{and} \quad \frac{\lambda_0}{2\lambda_p}\frac{z_d}{r_d} \ll 1. \tag{18}$$

These observations considerably reduce our diffraction integral in Eq. (14) to just

$$\mathbf{E}_d(\mathbf{r}_d) \approx \frac{\alpha}{45\lambda_p^2 r_d}\frac{I_0}{I_{\mathrm{cr}}}E_p(\mathcal{V}_3 + \mathcal{V}_4)\,\mathbf{u}_3. \tag{19}$$

The full Fresnel-like diffraction integral that couples the x, y, and z coordinates together, is unwieldy when attempting to garner qualitative information. By assuming $\xi_x \ll 1$, the Fresnel integral will produce a diffraction pattern with the same shape as if we took the Fourier limit. In this way, by performing the integral in x in $\mathcal{V}_3$ and $\mathcal{V}_4$, we obtain, for the diffracted field intensity $I_d(\mathbf{r}_d,\omega_p) = |\mathbf{S}_d(\mathbf{r}_d,\omega_p)|$, that

$$\begin{aligned} I_d(x_d,y_d,z_d = 0,\omega_p) &\\ &\sim I_{p,0}\exp\left[-\frac{(x_d/r_d)^2}{2\sigma_{d,x}^2}\right]\cos^2[\omega_p a(x_d/r_d)],\\ \sigma_{d,x}^2 := \frac{\lambda_p\sqrt{2}}{\pi w_{0,0}}, & \end{aligned} \tag{20}$$

with $I_{p,0} = E_p^2/2$, which is what one would expect from the Fourier transform of a Gaussian convoluted with two δ functions. The cosine term originates from the interference between the vacuum current generated in the two slits, and the Gaussian is the effect of the single-slit shapes of both strong beams. We use the $\sim$ sign to emphasize the illustrative nature of our arguments. Although the fringe positions are correctly predicted, the single-slit shape is incorrect, as seen in Fig. 2. This is an example of a consequence of nontrivial beam geometry, for which the full three-dimensional integration must be performed.

2. Analysis of field diffracted onto the z axis

An example of a diffraction pattern in the z direction is shown in Fig. 3. The numerical parameters are those used in the previous case but with $a/w_{0,0} = 0$ and now the reverse situation $x_d = 0$ and $z_d \ll y_d$. From this figure, we

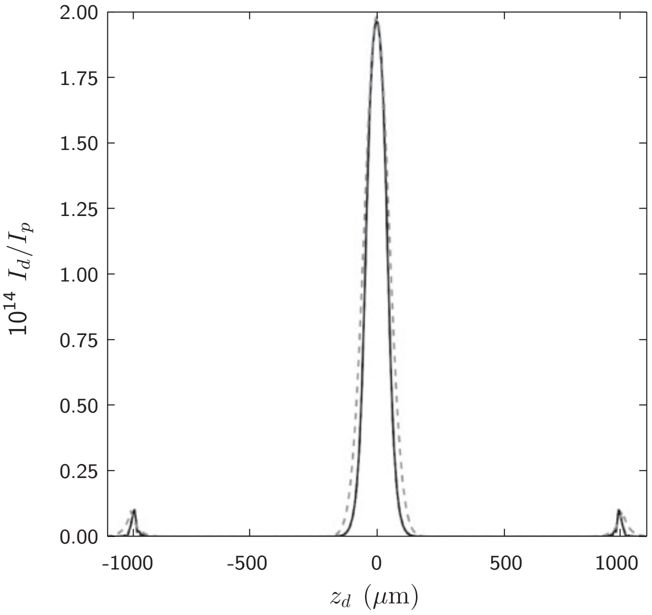

FIG. 3. The one-dimensional diffracted field along the z axis (i.e., along the axis of propagation of the strong-field beams) predicted by first-order QED theory is plotted with a solid line for the same physical parameters as in Fig. 2 but now with $a/w_{0,0} = 0$. The dotted line represents the simplified analytical approach by keeping quadratic terms in the exponential, described in the text.

see that the intensity pattern is formed by a central peak of width $\approx 50\ \mu$m and two smaller exponential-shaped peaks some distance away. Concerning the central peak, when we consider that the amplitude of the strong field along the z axis, and hence the "vacuum transmission aperture" are governed by the factor $1/[1 + (z/z_{r,0})^2]$, we see very clearly that the diffracted electromagnetic field does not result from the aperture's Fourier transform, which would have been a decaying exponential, symmetric about the origin (i.e., the wrong shape and with a smaller width of about 10 μm). The presence of the two peaks can be described by the diffraction-grating-like sinusoid along the z axis. That the simple Fourier analysis applied in the previous case does not work here, is already clear from the diffraction parameter $\xi_z \sim 25$, which is not smaller than unity.

Again, we wish to explain our diffracted field qualitatively, but this time how it, and hence Eq. (14), depends upon the z coordinate in the detector plane, z_d. We can see from Eq. (A1) how the decay of the integrand in the z direction is controlled by the soft core $1/[1 + (z/z_{r,0})^2]$ term. The importance and the presence of this term prevents us from separating out the z from the x and y integration variables and hence the z_d from the x_d and y_d detector-plane coordinates in the integrands $\mathcal{V}_k$, as we managed to do in the previous case. However, if we consider that $x_d = 0$ and that $z_d \ll y_d$, we can again neglect in Eq. (13) the terms proportional to the vectors $\mathbf{u}_1$ and $\mathbf{u}_2$. Unlike the previous situation, however, the condition Eq. (18) to neglect the integrals $\mathcal{V}_1$ and $\mathcal{V}_2$ is not fulfilled for arbitrary $z_d \ll r_d$, and they are accordingly not negligible. It can be shown, by performing an analysis similar to the one in the previous case, that the integrals $\mathcal{V}_3$ and $\mathcal{V}_4$ give rise to the central peak (with width $w_{p,0}/2 = 50\ \mu$m), while the integrals $\mathcal{V}_1$ and $\mathcal{V}_2$ give rise to the secondary smaller peaks located at $z_d = \mp 2 r_d \lambda_p/\lambda_0 = \mp 1000\ \mu$m. Therefore, the secondary peaks originate from the standing wave of the strong field, which the probe experiences as if it were a diffraction grating, and is another example of the effect of nontrivial beam shape. Similar arguments that lead to Eq. (20), which retain the quadratic terms in the exponential give the dashed line in Fig. 3 and again show good agreement.

3. Single-slit pattern

We have now seen from some results that a consequence of the nontrivial strong-field beam shape is a deviation from the ideal double-slit analogy. As mentioned in Sec. I, this mainly affects the interpretation of each strong-field laser as a single slit. We can illustrate the difference brought about by smooth edges when we consider diffraction from a single slit of dimension $2l_x \times 2l_z$ centered at the origin. The diffracted electric field in the far field $E_{d,\mathrm{Rect}}$ can be calculated via Fourier transformation of the aperture function,

$$E_{d,\mathrm{Rect}} \propto \int_{-\infty}^{\infty} dx \int_{-\infty}^{\infty} dz \exp\left(-i\omega\frac{x_d}{r_d}x - i\omega\frac{z_d}{r_d}z\right) \times \mathrm{Rect}\left(\frac{x}{l_x}\right)\mathrm{Rect}\left(\frac{z}{l_z}\right), \tag{21}$$

where Rect(x/a) equals unity only in the region $x \in]-a,a[$, otherwise being zero. This gives a diffracted intensity $I_{d,\mathrm{Rect}} \propto |E_{d,\mathrm{Rect}}|^2$,

$$I_{d,\mathrm{Rect}} \propto \frac{\sin^2(\omega x_d/r_d)}{(\omega x_d/r_d)^2}\frac{\sin^2(\omega z_d/r_d)}{(\omega z_d/r_d)^2}, \tag{22}$$

which gives the familiar single-slit minimum conditions $(n + 1/2)\lambda = 2l_x x_{d,n}/r_d$, $(n + 1/2)\lambda = 2l_z z_{d,n}/r_d$, for $n \in \mathbb{Z}$ and $\lambda = 2\pi/\omega$. For our Gaussian slits, our diffracted electric field $E_{d,\mathrm{Gauss}}$ becomes

$$E_{d,\mathrm{Gauss}} \propto \int_{-\infty}^{\infty} dx \int_{-\infty}^{\infty} dz \exp\left(-i\omega\frac{x_d}{r_d}x - i\omega\frac{z_d}{r_d}z\right) \times \exp\left(-\frac{x^2}{w_{0,0}^2(1+z^2)}\right)\frac{1}{1+z^2}. \tag{23}$$

This can be analytically evaluated after setting $z_d = 0$, giving an intensity,

$$I_{d,\mathrm{Gauss}} \propto \exp\left[-\left(\frac{\omega w_{0,0} x_d}{2r_d}\right)^2\right] K_0^2\left[\frac{1}{2}\left(\frac{\omega w_{0,0} x_d}{2r_d}\right)^2\right], \tag{24}$$

where K_0 is the zeroth-order modified Bessel function of the first kind and is monotonically decreasing (i.e., without fringe structure). As other terms introduce only a finer structure and as the final integration in y would also be over a smooth function, we see that no periodicity arises from our single-slit diffraction pattern, which is consistent with numerical results. Beyond the far-field limit, however, a deviation displaying interference behaviour would be expected to develop. One example of this was calculated in Ref. [51], where a relativistic Gaussian electron wave packet in the Coulomb field of some highly charged ions acquires an interference pattern structure when placed in an intense laser field.

4. Resultant intensity difference off axis

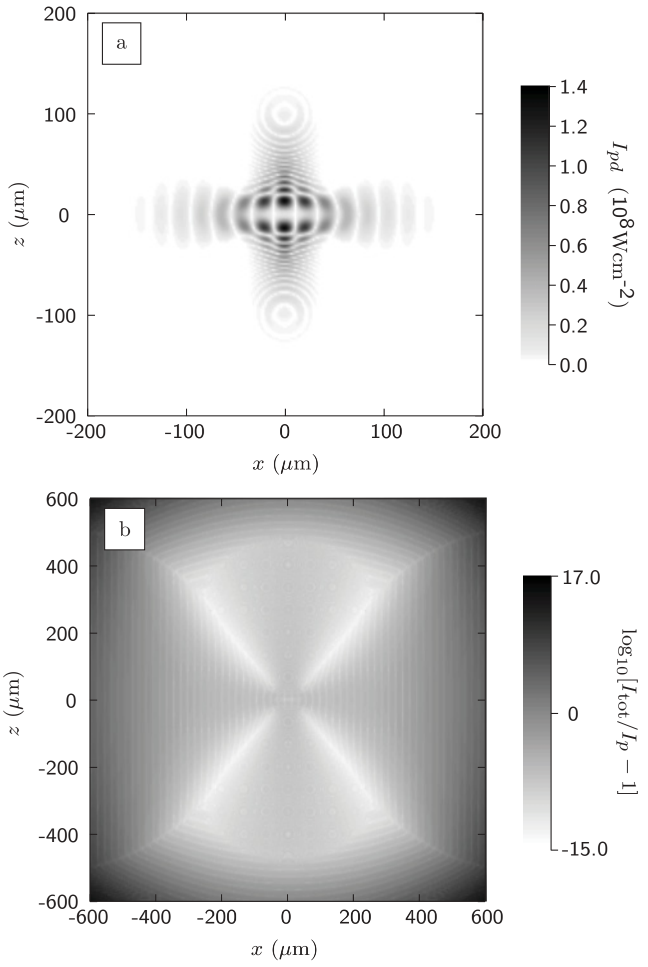

FIG. 4. Plot (a) is of the quantity I_{pd}, the vacuum-probe cross term in time-averaged total intensity, at a distance $r_d \approx y_d = 1$ m, with the same experimental parameters as in the example of diffraction along the x axis apart from $a/w_{0,0} = 12$. Plot (b) is the logarithm to base 10 of this divided by the time-averaged probe intensity (i.e., the logarithm of the signal-to-noise ratio for the same parameters).

For the relevance to experiment, however, instead of just plain diffraction theory, we will be more interested in studying the *difference* brought about by vacuum polarization effects. With $\langle\rangle$, which denotes an average over a laser cycle, the difference can be shown to be

$$\begin{aligned} I_{\mathrm{tot}} - I_p &= (\langle|\mathbf{E}_p + \mathbf{E}_d|^2\rangle - \langle|\mathbf{E}_p|^2\rangle) \\ &= I_{pd} + I_d, \end{aligned}$$

$$\begin{aligned} I_{pd} = \frac{I_0}{I_{\mathrm{cr}}}\frac{\alpha I_{p,0}}{180\pi\lambda_p^2}\,\frac{\exp\left[-\left(x_d^2+z_d^2\right)/w_p^2\right]}{y_d\sqrt{1+(y_d/y_r)^2}} \\ \times(\mathcal{V}^i\sin\eta - \mathcal{V}^r\cos\eta)\cdot(\hat{\mathbf{x}}\cos\theta + \hat{\mathbf{z}}\sin\theta), \end{aligned} \quad (25)$$

$$I_d = \langle|E_d|^2\rangle; \quad (26)$$

$$\mathcal{V}^r := \mathrm{Re}(\mathcal{V}), \quad \mathcal{V}^i := \mathrm{Im}(\mathcal{V}), \quad (27)$$

$$\mathcal{V} = (\mathcal{V}_1 + \mathcal{V}_2)\,\mathbf{u_1} + (\mathcal{V}_3 - \mathcal{V}_4)\,\mathbf{u_2} + \left(\sum_{i=1}^{4}\mathcal{V}_i\right)\mathbf{u_3}, \quad (28)$$

$$\eta = \tan^{-1}\left(\frac{y_d}{y_r}\right) - \frac{\omega_p y_d}{2}\frac{x_d^2+z_d^2}{y_r^2+y_d^2}. \quad (29)$$

We evaluate this expression on an x_d-z_d grid at a fixed distance y_d and calculate the differences in photon rates brought about by the polarized vacuum. Our procedure was to make many such grids that became ever finer so that we could see how the integral and therefore the predicted number of photons per shot, converged. Since the diffraction pattern must be smooth, this number should then yield a reliable value. We took the same following parameters of a typical experimental run: $y_d = 1$ m, $a/w_{0,0} = 12, b/w_{0,0} = 0, w_{0,0} = \lambda_0 = 0.8$ μm and $I_0 = 10^{24}$ W cm^{-2}, which gives the patterns shown in Fig. 4(a) (the parameters of the probe field were those already employed in the previous examples). We focus on the diffracted photons described by the interference term between $\mathbf{E}_p(\mathbf{r}_d,t)$ and $\mathbf{E}_d(\mathbf{r}_d,t)$. This term spreads out in the x-z plane with a width $\sqrt{2}$ larger than that for the probe field, as the multiplying diffraction signal has a much wider overall decay, so there exist regions in which the ratio of the diffracted-to-probe signal is favorable, which can be seen on the log plot of the total difference due to vacuum signal over the probe background Fig. 4(b). At the same time, moving too far from the center of the pattern will reduce the intensity to the point where nothing can be detected. If we consider drilling a hole of radius ρ into the center of the detector and approximate the decay of I_{pd} to come entirely from the probe Gaussian, by considering the single strong-beam scenario in order to maximize the signal, we can obtain limits on ρ,

$$\left[\ln\frac{N_p}{N_{pd}}\right]^{1/2} \lesssim \frac{\rho}{w_p(y)} \lesssim [\ln N_{pd}]^{1/2} \quad (30)$$

for the total incident probe and cross-term diffracted photons N_p,N_{pd}. This agrees with the intuitive notion that, to stand any chance of measurement, the signal must be larger than statistical noise from the background, which if modeled with Poisson statistics, implies $N_{pd} > \sqrt{N_p}$.[2] We can either fulfill this condition that the vacuum signal is larger than the minimum background noise over the entire plate, or we can consider measuring counts only in regions where $N_{pd}(\rho) \gtrsim N_p(\rho)$. In both cases, the number of diffracted photons will simply increase with probe intensity, whereas as N_p depends only on the probe laser energy and wavelength λ_p, and so, for larger probe intensity, we can easier fulfill both bounds on ρ in Eq. (30). First, setting $y_d = 50$ cm and the still, at ELI, comfortably attainable $I_0 = 5 \times 10^{24}$ W cm^{-2}, for a probe focal width of 8 μm, we achieve $N_{pd} = 7.5 \times 10^7$ from $N_p = 8.0 \times 10^{12}$ probe photons per shot. Second, we can plot how $N_{pd}(\rho)$ varies with the hole radius, and for a tighter probe-beam focal width of $w_{p,0} = 3.6$ μm (recent results from the LCLS include focusing down to 0.12 nm [52]),

---

[2] When the statistical error in the number of photons is modeled by a Poisson distribution, the relative error in the mean photons measured per shot μ is given by $1/\sqrt{n\mu}$ for n shots. As long as lower intensity lasers still satisfy the condition $N_{pd} > \sqrt{N_p}$, they can indeed be used, it is just a question of how long the experiment can be run to make $n\mu$ large enough to be certain to have observed an effect.

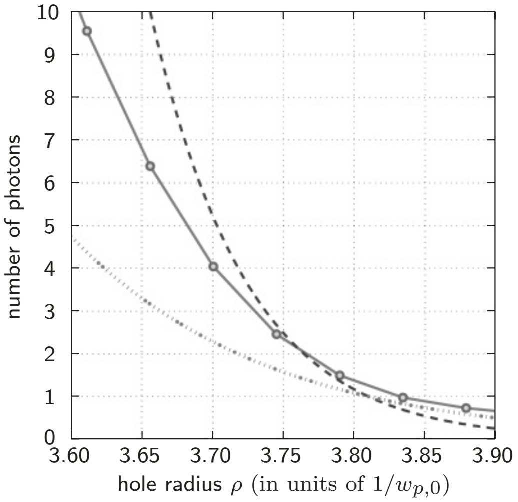

FIG. 5. For a probe beam focused at $w_{p,0} = 3.6\ \mu$m, $w_p(y_d) = 5.0\ \mu$m, and a large enough detector hole radius ρ, the photon count from the vacuum-probe cross term $N_{pd}(\rho)$ (solid line) becomes comparable to that from the probe $N_p(\rho) = N_p(0)\exp\{-2[\rho/w_p(y_d)]^2\}$ (dashed line) (here, around two diffracted photons) and greater than statistical noise from the probe $\sqrt{N_p(\rho)}$ (dotted line).

we expect to be attainable in the near future, we achieve the dependency shown in Fig. 5. In the region $N_{pd}(\rho) \gtrsim N_p(\rho)$, by taking the efficiency of commercially available charge-coupled devices for $\lambda_p = 0.4$ nm or 3.1-keV photons ($\gtrsim 90\%$ [53]) into account, we expect approximately two diffracted photons to be measurable per shot of the probe beam. This can then be compared with results for I_d which, by not being subjected to the probe Gaussian envelope, has a much wider spread, and is possibly easier to measure as reported in Ref. [37], with the caveat that an optical probe beam was used with a total energy 2.5×10^3 larger than in the present x-ray case.

B. Polarization results (double slit)

This section concerns itself with the induced ellipticity and rotation of the probe polarization due to VPEs, which can be measured on the probe beam's propagation axis. By setting $x_d = z_d = 0$, it can be shown that new expressions that incorporate defocusing terms in the probe, for the polarization ψ and ellipticity ε, are given by

$$\psi = \frac{\alpha \sin 2\theta}{120\lambda_p^2}\frac{I_0}{I_{\mathrm{cr}}}\sum_{k=1}^{4}\left(\frac{\mathcal{V}_k^i}{y_{r,p}}+\frac{\mathcal{V}_k^r}{y_d}\right), \tag{31}$$

$$\varepsilon = \frac{\alpha \sin 2\theta}{120\lambda_p^2}\frac{I_0}{I_{\mathrm{cr}}}\sum_{k=1}^{4}\left(\frac{\mathcal{V}_k^r}{y_{r,p}}-\frac{\mathcal{V}_k^i}{y_d}\right), \tag{32}$$

where in the limit of $a,b, \to 0$, $y_{r,p} \to \infty$, we again recover the expression in the original paper [40]. We also note that the introduction of experimentally relevant defocusing terms in the probe produces the more realistic and expected result that $\lim_{y_d\to\infty}\{\psi,\varepsilon\} \neq \{0,0\}$.

By varying y_d with $x_d/r_d, z_d/r_d = 0$ and setting $\theta = \pi/4$ to maximize the effect of the polarized vacuum, we show a demonstrative plot in Fig. 6, for how ψ and ε vary for a fixed strong-field beam separation $a/w_{0,0} = 12$, with the other parameters the same as in the previous examples. The first difference we note is that, in comparison with results from Ref. [40], for $y_d \ll y_{r,p}$, polarization and ellipticity oscillate rapidly, and there are sizable ranges where both are larger than that for previously derived results. For the choice of parameters in the plot, $y_{r,p} \approx 80$ m, and so, if we keep within this range (i.e., disregard the effect of probe defocusing terms), we can clearly ascertain the improvement brought by separating the strong-field beams. This perhaps counterintuitive result can be shown to be consistent with our analysis by following through these conditions on the detector-plane coordinates and studying the form of the integrals $\mathcal{V}_{3,4}$ that appear in our expressions for ψ and ε (we can once more disregard the contribution of $\mathcal{V}_{1,2}$):

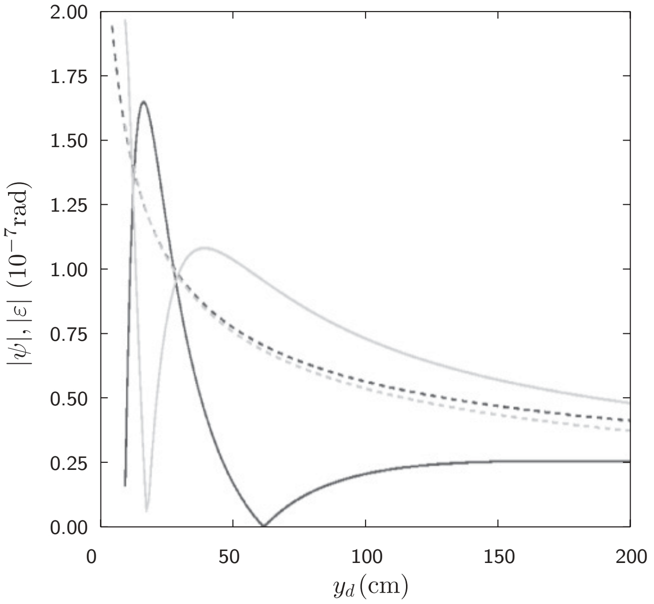

FIG. 6. The absolute value of the new polarization and ellipticity expressions derived with probe defocusing terms and separated strong-field beams as a function of the observation distance y_d, for the same parameters as in Fig. 2 but with $a/w_{0,0} = 12$. The dashed lines are the former analytical polarization and ellipticity formulas for $a = 0$ without probe defocusing terms, given in Ref. [40], with the solid lines as the new polarization and ellipticity presented in this paper. Darker lines are drawn for polarization rotation and lighter ones for ellipticity.

$$\mathcal{V}_{3,4} = \int_{-\infty}^{\infty} dz\, \frac{1}{1+(z/z_{r,0})^2} \times \exp\left(-i\omega_p\frac{z^2}{2y_d} - \frac{z^2}{w_{p,0}^2}\right)\mathcal{I}_{y,\pm}\mathcal{J}_{x,\pm}, \tag{33}$$

$$\mathcal{I}_{y,\pm} = \int_{-\infty}^{\infty} dy\, \exp\left(\frac{-2(y-b)^2}{w_0^2}\right), \tag{34}$$

$$\mathcal{J}_{x,\pm} = \int_{-\infty}^{\infty} dx\, \exp\left(-i\omega_p\frac{x^2}{2y_d}\right)\exp\left(-\frac{x^2}{w_{p,0}^2}\right) \times \exp\left(\frac{-2(x\mp a)^2}{w_0^2}\right). \tag{35}$$

From Eq. (34), we can see more clearly, that under these conditions [especially as $y_{r,p} \gg 2(w_{0,0} + b)$], since there is no other structure in the y direction, b becomes an inconsequential parameter when measuring polarization and ellipticity, just as it was for the diffracted field, and will likewise be set to zero. By separating strong-field beams in the x direction, we see that we only produce an effect on the x integrals $\mathcal{J}_{x,\pm}$. When considering the contribution from the first complex exponential factor in Eq. (35), for a fixed a, in varying y_d, we vary the overlap this factor's real cosine and imaginary sine functions with the other two Gaussian integrand factors, which have maxima at $x = 0$ and $x = \mp a$, respectively. Hence, some values of y_d form local maxima in ψ and ε, and due to the trigonometric nature of the varying function, we have the oscillating shape in Fig. 6. However, in the limit $y_d \to 0$ (by taking all $\mathcal{V}$'s into account), both of these values tend to constants:

$$\psi = 0, \quad \varepsilon = \frac{\alpha\sqrt{\pi}}{30\sqrt{2}} \frac{I_0}{I_{\rm cr}} \frac{w_{0,0}}{\lambda_p} \exp\left(\frac{-2a^2}{w_{0,0}^2}\right) \sin 2\theta. \tag{36}$$

We also show how ψ and ε depend upon beam separation a in Fig. 7 and can show consistency by using the same arguments as earlier for the dependence on y_d. In varying a, the first two factors in Eq. (35) act as fixed peaks, whereas the final Gaussian term is moved to place its peak $x = \mp a$, at such a position that could be used to maximize the integral. We recall from Eqs. (31) and (32), that ψ and ε contain mixtures of both the real and imaginary parts of this integral. When considering the contribution from the imaginary part of the integrand, we see that the maximum of the first complex exponential factor (i.e., of the sinusoidal) will not occur at the origin, unlike that of the second Gaussian factor, and, hence, in order to maximize this integral, which comprises three functions, we should place the peak of the third function somewhere between the peaks of the first two, which corresponds to a value $a \neq 0$. Moreover, as the first sinusoidal factor is periodic and has a wavelength much smaller than the width $w_{p,0}$ of the Gaussian that multiplies it, we should have a series of maxima in both $\psi(a)$ and $\varepsilon(a)$ that decay slowly with a (see Fig. 7). For the case $y_d \ll y_{r,p}$, our explanation would, on one hand, predict that the value of $\varepsilon(a)$ would initially rise as a increases, and on the other hand, would justify the maximum of $\psi(a)$, which is very close to the origin, and hence that $\psi(a)$ would decrease as a initially increases from 0. These results can be further confirmed via differentiation under the integral in Eq. (33) and are exactly what we observe in the numerical evaluation depicted in Fig. 7. This increase is another reflection of the role of Fresnel terms in a nontrivial beam geometry. From numerical analysis, the polarization and ellipticity were found to increase by a factor of 1.4 over $a = 0$ values.

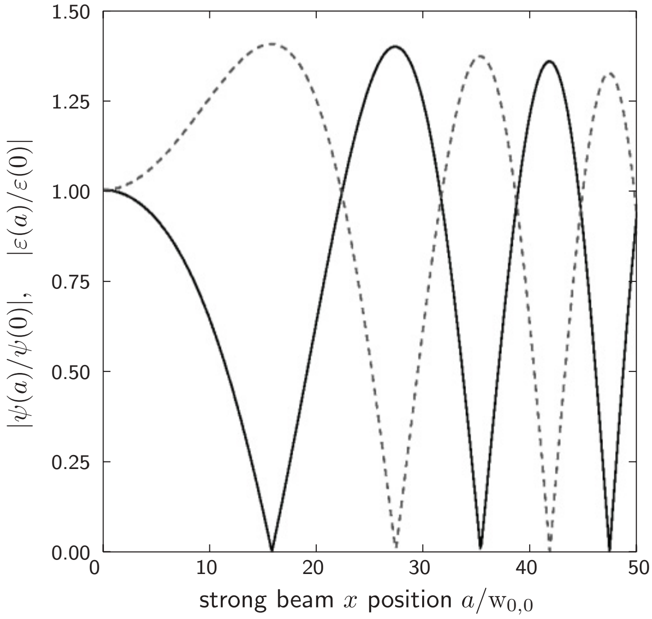

FIG. 7. The ratios of $|\psi(a)/\psi(0)|$ (continuous line) and $|\varepsilon(a)/\varepsilon(0)|$ (dashed line) in the double-slit setup for the same parameters as in Fig. 2 but with $w_{p,0} = 200$ μm. The ratio $|\psi(a)/\psi(0)|$ was chosen in preference to the ratio of $|\psi(a)|$ with that in the original paper [40] because the introduction of defocusing terms does not make the latter a viable comparison.

C. Polarization results (single shaft)

Here, we briefly want to consider a different field configuration, in which the strong beams propagate parallel and antiparallel to the probe field. In this experimental setup, we exchange the coordinates y and z in the expressions for the strong fields in Eq. (5), gaining a corresponding y-axis strong-field Rayleigh length $y_{r,0}$ and Gouy phase $\phi_{g,0} = \tan^{-1}(y/y_{r,0})$. To the probe field, we add defocusing terms inside the integral, which would allow us to consider the case $w_{p,0} < w_{0,0}$. The diffracted field $\mathbf{E}_d(\mathbf{r}_d)$ is then given by the following expression:

$$\mathbf{E}_d(\mathbf{r}_d) := \frac{I_0}{I_{\rm cr}} \frac{\alpha E_p}{45\lambda_p^2 r_d}[2\mathcal{V}_1'\mathbf{u}_1' + (\mathcal{V}_3' + \mathcal{V}_4')\,\mathbf{u}_{34}'], \tag{37}$$

$$\begin{aligned}\mathcal{V}_k' := \int_{-\infty}^{\infty} d^3r \exp\Bigg[i\omega_p\Bigg(&\frac{x^2+y^2+z^2}{2r_d} - \frac{xx_d + yy_d + zz_d}{r_d} \\ &- \frac{(xx_d+yy_d+zz_d)^2}{2r_d^3} + y\Bigg) - \frac{x^2+z^2}{w_p^2} \\ &- \frac{2}{w_0^2}(x^2+z^2+a^2+b^2) + \frac{i\omega_p y(x^2+z^2)}{2\left(y^2+y_{r,p}^2\right)} \\ &- i\tan^{-1}\left(\frac{y}{y_{r,p}}\right)\Bigg] \frac{\mathcal{I}_k'}{1+(y/y_{r,0})^2} \frac{1}{\sqrt{1+(y/y_{r,p})^2}},\end{aligned} \tag{38}$$

$$\mathcal{I}_1' := \exp\left(-\frac{4}{w_0^2}(xa+zb)\right),$$

$$\begin{aligned}\mathcal{I}_3' := \exp\Bigg[2i\Bigg(&\omega_0 y - \tan^{-1}\frac{y}{y_{r,0}} \\ &+ \frac{\omega_0 y(x^2+z^2+a^2+b^2)}{2\left(y^2+y_{r,0}^2\right)}\Bigg) + i\Delta\psi_0\Bigg],\end{aligned} \tag{39}$$

$$\begin{aligned}\mathcal{I}_4' := \exp\Bigg[-2i\Bigg(&\omega_0 y - \tan^{-1}\frac{y}{y_{r,0}} \\ &+ \frac{\omega_0 y(x^2+z^2+a^2+b^2)}{2\left(y^2+y_{r,0}^2\right)}\Bigg) - i\Delta\psi_0\Bigg],\end{aligned}$$

where we have also introduced a phase difference term $\Delta\psi_0 = \psi_{0,2} - \psi_{0,1}$ between the absolute phases of the two strong beams, which turns out to have a negligible effect for the same reasons as separating the beams in the longitudinal direction and is correspondingly set to zero. The vectors $\mathbf{u}'_1$ and $\mathbf{u}'_{34}$ are

$$\mathbf{u}'_1 := \begin{bmatrix} \left(1+\frac{y_d}{r_d}\right)\cos\theta + \frac{x_d}{r_d}\left(\frac{x_d}{r_d}\cos\theta + \frac{7}{4}\frac{z_d}{r_d}\sin\theta\right) \\ -\frac{7}{4}\frac{z_d}{r_d}\sin\theta + \frac{y_d}{r_d}\frac{x_d}{r_d}\cos\theta + \frac{7}{4}\frac{y_d}{r_d}\frac{z_d}{r_d}\sin\theta \\ \frac{7}{4}\frac{y_d}{r_d}\sin\theta + \frac{x_d}{r_d}\frac{z_d}{r_d}\cos\theta + \frac{7}{4}\left[\left(\frac{z_d}{r_d}\right)^2 + 1\right]\sin\theta \end{bmatrix}, \tag{40}$$

$$\mathbf{u}'_{34} := \begin{bmatrix} 2\left(1-\frac{y_d}{r_d}\right)\cos\theta + 2\left(\frac{x_d}{r_d}\right)^2\cos\theta + -\frac{3}{4}\frac{x_d}{r_d}\frac{z_d}{r_d}\sin\theta \\ 3\frac{x_d}{r_d}\cos\theta - \frac{3}{4}\frac{z_d}{r_d}\sin\theta\left(\frac{y_d}{r_d}+1\right) + 2\frac{x_d}{r_d}\frac{y_d}{r_d}\cos\theta \\ \frac{3}{4}\left(\frac{y_d}{r_d}-1\right)\sin\theta + 2\frac{x_d}{r_d}\frac{z_d}{r_d}\cos\theta - \frac{3}{4}\left(\frac{z_d}{r_d}\right)^2\sin\theta \end{bmatrix}. \tag{41}$$

As in the previous case, we set $(x_d/r_d),(z_d/r_d) \to 0,(y_d/r_d) \to 1$ in Eqs. (40) and (41), which removes the latter vector completely, effectively eliminating any contribution from $\mathbf{E}_{0,2}(\mathbf{r},t)$, the strong-field beam with a wave vector parallel to that of the probe. This result then coincides with the general property of a plane wave that it does not polarize the vacuum. In this geometry, we obtain, for the polarization ψ and the ellipticity ε, the following expressions:

$$\psi = \frac{\alpha \sin 2\theta}{15\lambda_p^2}\frac{I_0}{I_{\rm cr}}\left(\frac{\mathcal{V}_1'^r}{y_d} + \frac{\mathcal{V}_1'^i}{y_{r,p}}\right), \tag{42}$$

$$\varepsilon = \frac{\alpha \sin 2\theta}{15\lambda_p^2}\frac{I_0}{I_{\rm cr}}\left(\frac{\mathcal{V}_1'^r}{y_{r,p}} - \frac{\mathcal{V}_1'^i}{y_d}\right). \tag{43}$$

We can compare these to existing results arrived at by Heinzl *et al.* [39] when we take $a = b = 0$ and the two limits: the *refractive-index* and the *crossed-field* limits. The first is obtained when we take $y_d \to 0$ (near region) in a regime where ψ becomes linear with y_d and, therefore, disappears, and ε converges to a constant. The crossed-field limit corresponds to a constant strong field (i.e., $\omega_0 \to 0$), which we can achieve when we let the counterpropagating pulse be, for example, of the form of a cosine. This ensures that neither the strong electric nor the magnetic field disappears in this limit so that we can keep the normalization used in Eqs. (42) and (43). To be consistent, the time-averaging procedure that removes evanescent waves must be repeated with the precondition that $\omega_0 = 0$. Then, Eq. (43) tends to the result in Ref. [39]:

$$\varepsilon = \frac{2\alpha\pi}{15}\frac{I_0}{I_{\rm cr}}\frac{y_0}{\lambda_p}\sin 2\theta, \quad y_0 = \frac{y_{r,p}y_{r,0}}{y_{r,p}+y_{r,0}}. \tag{44}$$

The only difference to the formula in Ref. [39] is that we have incorporated the focusing of the strong and probe fields, which automatically generates the effective interaction length y_0 of the beams.

Another feature that is different here, is that we allow the strong-field wave to be positioned off axis. We showed and explained how this increases the ellipticity and polarization in the double-slit setup, and in this single-shaft experiment with just one beam, one acquires a similar result (see Fig. 8). For the same experimental parameters as in Fig. 2 but with $y_d = 50$ cm and $a/w_{0,0} = 10$, we achieve a modest increase in the ellipticity of 1.3 over single strong-beam values. We mention here that one could also form a double-shaft geometry, which leads to the same relative increase as for the off-axis single-shaft one. As $x_d = z_d = 0$, this can be understood as a result of the symmetry of the setup, which can also be seen in Eq. (38), which is symmetric in x and a in this limit.

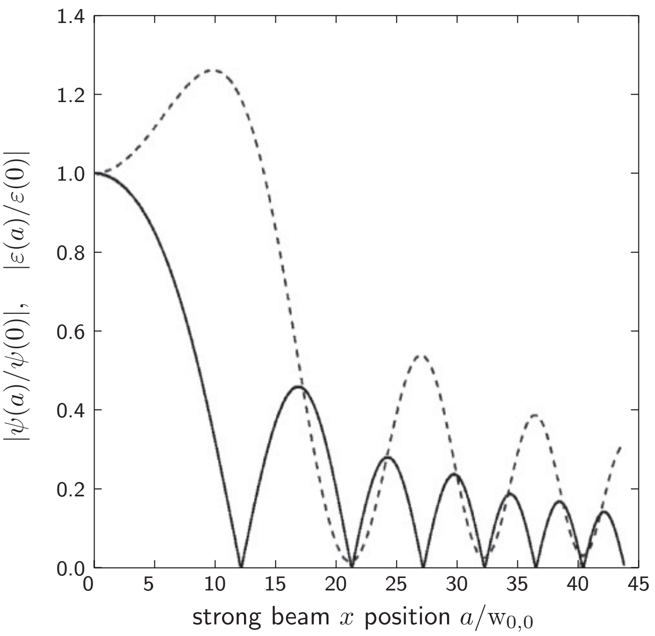

FIG. 8. The ratios of $|\psi(a)/\psi(0)|$ (continuous line) and $|\varepsilon(a)/\varepsilon(0)|$ (dashed line) in the single-shaft setup for the same experimental parameters as in Fig. 2 but with $y_d = 50$ cm.

IV. CONCLUSION

The main focus of this paper was to extend the results derived in Ref. [40] to incorporate more features applicable to experiment. One development has been to extend into the far-field region, the range in which polarization rotation and ellipticity formulas are valid. These results were calculated for two different geometries: double slit and single or double shaft. Another addition has been to include a separation of the strong-field beams. This nontrivial beam geometry, in conjunction with higher-order Fresnel diffraction terms, was shown to increase polarization rotation and ellipticity values for a range of beam parameters in the double slit case by a factor of 1.4 and, in the single or double shaft case, by a factor of 1.3. Although these increases are relative to the values at zero beam separation, we acknowledge that, since the overall accuracy of the calculation is $\approx 1/\pi$, some care should be taken in interpreting these results [calculations performed after submission with a larger $w_{0,0}$ (e.g., $w_{0,0} = 5\lambda_0$) show that the effect both persists and is larger than the corresponding accuracy of the order of $\lambda_0/\pi w_{0,0}$]. By calculating the diffraction pattern that results from the interference between the polarized vacuum and probe signals, we have illuminated another possible route for measuring laser-induced VPEs. For experimental parameters comfortably attainable at the upcoming XFEL and ELI facilities, we have shown how approximately 10^{-5} of the incident photons can be diffracted with around two photons per shot of the lasers that are diffracted into regions where the vacuum signal is higher than the probe background. However, we stress that an increase would also be observed by using ELI with a tabletop x-ray laser such as, for example, in Ref. [54], where a beam of frequency 29 nm was used. These, in principle, measurable diffraction vacuum polarization effects, would be evidence of nonlinear vacuum polarization in laser fields.

ACKNOWLEDGMENT

We acknowledge helpful discussions with J. Crespo Lopez-Urrutia.

APPENDIX

The volume integral from Eq. (15) can be integrated in the x and y coordinates to give

$$\begin{aligned}\mathcal{V}_k = \int_{-\infty}^{\infty} dz \frac{\pi w_{0,0}^2}{\sqrt{\alpha_x\alpha_y}} \frac{1}{1+(z/z_{r,0})^2}\\
\times \exp\Bigg(\frac{\pi^2}{\alpha_y}\left(\frac{w_{0,0}}{\lambda_p}\right)^2 \Bigg[i\frac{y_d}{r_d}\left(1+\frac{zz_d}{r_d^2}\right) + i\frac{\pi}{\alpha_x}\frac{x_d y_d}{r_d^2}\frac{w_0^2}{r_d\lambda_p}\\
\times\left(\frac{ix_d}{r_d}+\frac{ix_d z_d z}{r_d^3}-\frac{\beta_k}{\pi}\frac{a\lambda_p}{w_0^2}\right)-\frac{\beta_k}{\pi}\frac{b\lambda_p}{w_0^2}-i\Bigg]^2\\
-\frac{z^2}{w_{p,0}^2}\left\{\frac{i\pi w_{p,0}^2}{\lambda_p r_d}\left[1-\left(\frac{z_d}{r_d}\right)^2\right]+1\right\}+\frac{4\pi}{\alpha_x}\left(\frac{w_{0,0}}{\lambda_p}\right)^2\\
\times\left[i\frac{x_d}{r_d}\left(1+\frac{zz_d}{r_d^2}\right)-\frac{\beta_k}{\pi}\frac{a\lambda_p}{w_0^2}\right]^2\\
+2\pi i\frac{z_d}{r_d}\frac{z}{\lambda_p}+4i\Gamma_k\pi\frac{z}{\lambda_0}\left(1+\frac{a^2+b^2}{2(z^2+z_{r,0}^2)}\right)\\
-2i\Gamma_k\phi_{g,0}(z)-\frac{2(a^2+b^2)}{w_0^2}\Bigg),\end{aligned}\tag{A1}$$

where we have defined

$$\begin{aligned}\alpha_x := i\pi\frac{w_{0,0}^2}{\lambda_p r_d}\left[1-\left(\frac{x_d}{r_d}\right)^2\right]+\frac{2}{1+(z/z_{r,0})^2}\\
-\frac{2i\Gamma_k z}{z_{r,0}}\frac{1}{1+(z/z_{r,0})^2}+\left(\frac{w_{0,0}}{w_{p,0}}\right)^2,\end{aligned}\tag{A2}$$

$$\begin{aligned}\alpha_y := i\pi\frac{w_{0,0}^2}{\lambda_p r_d}\left[1-\left(\frac{y_d}{r_d}\right)^2\right]+\frac{2}{1+(z/z_{r,0})^2}\\
-\frac{2i\Gamma_k z}{z_{r,0}}\frac{1}{1+(z/z_{r,0})^2}+\frac{\pi^2}{\alpha_x}\left(\frac{x_d y_d}{r_d^2}\frac{w_0^2}{r_d\lambda_p}\right)^2,\end{aligned}\tag{A3}$$

and have included all four integrals with

$$\Gamma_k = \begin{cases} 1 & \text{if } k=1,\\ -1 & \text{if } k=2,\\ 0 & \text{if } k=3,4,\end{cases} \quad\text{and}\quad \beta_k = \begin{cases} 0 & \text{if } k=1,2,\\ 1 & \text{if } k=3,\\ -1 & \text{if } k=4.\end{cases}\tag{A4}$$

---

[1] W. Heisenberg and H. Euler, Z. Phys. **98**, 714 (1936).
[2] V. Weisskopf, Mat. Fys. Medd. K. Dan. Vidensk. Selsk. **14**, 6 (1936).
[3] F. Sauter, Z. Phys. **69**, 742 (1931).
[4] N. B. Narozhny *et al.*, Phys. Lett. A **330**, 1 (2005).
[5] A. R. Bell and J. G. Kirk, Phys. Rev. Lett. **101**, 200403 (2008).
[6] J. G. Kirk, A. R. Bell, and I. Arka, Plasma Phys. Controlled Fusion **51**, 085008 (2009).
[7] G. V. Dunne, H. Gies, and R. Schützhold, Phys. Rev. D **80**, 111301(R) (2009).
[8] E. I. Guendelman, Phys. Lett. B **662**, 445 (2008).
[9] M. Ahlers, H. Gies, J. Jaeckel, J. Redondo, and A. Ringwald, Phys. Rev. D **77**, 095001 (2008).
[10] M. Ahlers, H. Gies, J. Jaeckel, J. Redondo, and A. Ringwald, Phys. Rev. D **76**, 115005 (2007).
[11] H. Gies, Eur. Phys. J. D **55**, 311 (2009).
[12] D. Tommasini *et al.*, J. High Energy Phys. 11 (2009) 043.
[13] W. Dittrich and M. Reuter, *Effective Lagrangians in Quantum Dynamics* (Springer-Verlag, Berlin, 1985).
[14] A. I. Milstein and M. Schumacher, Phys. Rep. **243**, 183 (1994).
[15] D. Bernard *et al.*, Eur. Phys. J. D **10**, 141 (2000).
[16] E. Lundström, G. Brodin, J. Lundin, M. Marklund, R. Bingham, J. Collier, J. T. Mendonça, and P. Norreys, Phys. Rev. Lett. **96**, 083602 (2006).
[17] G. Brodin, M. Marklund, and L. Stenflo, Phys. Rev. Lett. **87**, 171801 (2001).
[18] D. Tommasini, A. Ferrando, H. Michinel, and M. Seco, Phys. Rev. A **77**, 042101 (2008).
[19] A. Ferrando, H. Michinel, M. Seco, and D. Tommasini, Phys. Rev. Lett. **99**, 150404 (2007).
[20] Y. I. Salamin *et al.*, Phys. Rep. **427**, 41 (2006).
[21] G. Mourou, T. Tajima, and S. Bulanov, Rev. Mod. Phys. **78**, 309 (2006).
[22] M. Marklund and P. K. Shukla, Rev. Mod. Phys. **78**, 591 (2006).
[23] J. T. Mendonca *et al.*, Phys. Lett. A **359**, 700 (2006).
[24] S. Z. Akhmadaliev *et al.*, Phys. Rev. Lett. **89**, 061802 (2002).
[25] G. Brodin, M. Marklund, B. Eliasson, and P. K. Shukla, Phys. Rev. Lett. **98**, 125001 (2007).
[26] A. Di Piazza, A. I. Milstein, and C. H. Keitel, Phys. Rev. A **76**, 032103 (2007).
[27] A. Di Piazza, K. Z. Hatsagortsyan, and C. H. Keitel, Phys. Rev. D **72**, 085005 (2005).
[28] A. M. Fedotov and N. B. Narozhny, Phys. Lett. A **362**, 1 (2006).
[29] A. I. Milstein, I. S. Terekhov, U. D. Jentschura, and C. H. Keitel, Phys. Rev. A **72**, 052104 (2005).
[30] F. Özel, T. Güver, and E. Göğüş, AIP Conf. Proc. **983**, 254 (2008).
[31] V. M. Kaspi, Astrophys. Space Sci. **308**, 1 (2007).
[32] V. I. Denisov and S. I. Svertilov, Astron. Astrophys. **399**, L39 (2003).
[33] M. G. Baring, AIP Conf. Proc. **1051**, 53 (2008).

[34] V. V. Usov, Astrophys. J **572**, L87 (2002).

[35] Y. J. Ding and A. E. Kaplan, Int. J. Nonlinear Opt. Phys. **1**, 51 (1991).

[36] E. Zavattini *et al.*, Phys. Rev. D **77**, 032006 (2008).

[37] B. King, A. Di Piazza, and C. H. Keitel, Nature Photon. **4**, 92 (2010).

[38] M. Marklund, Nature Photon. **4**, 72 (2010).

[39] T. Heinzl *et al.*, Opt. Commun. **267**, 318 (2006).

[40] A. Di Piazza, K. Z. Hatsagortsyan, and C. H. Keitel, Phys. Rev. Lett. **97**, 083603 (2006).

[41] V. Yanovsky *et al.*, Opt. Express **16**, 2109 (2008).

[42] European Light Infrastructure (ELI), *ELI Scientific Case* [http://www.extreme-light-infrastructure.eu/Publications_2_4.php].

[43] High Power laser Energy Research (HiPER), *HiPER Technical Background and Conceptual Design Report*, [http://www.hiperlaser.org/docs/tdr/HiPERTDR2.pdf].

[44] Z. Major *et al.*, in *OPA Development on the Petawatt Field Synthesizer*, Advanced Solid-State Photonics, OSA Technical Digest Series (CD) (Optical Society of America, Washington, DC, 2009), paper MB5.

[45] A. Ringwald, Phys. Lett. B **510**, 107 (2001).

[46] X-Ray Free-Electron Laser (XFEL), *The European X-Ray Free-Electron Laser Technical Design Report* [http://xfel.desy.de/tdr/tdr] (2007).

[47] Stanford Linear Accelerator Center and Lawrence Livermore National Laboratory and Argonne National Laboratory, *Linac Coherent Light Source (LCLS)* [http://lcls.slac.stanford.edu/] (2009).

[48] L. Levi, *Applied Optics* (Wiley, New York, 1968).

[49] W. Dittrich and H. Gies, *Probing the Quantum Vacuum* (Springer-Verlag, Berlin, 2000).

[50] J. D. Jackson, *Classical Electrodynamics* (Wiley, New York, 1975).

[51] G. R. Mocken and C. H. Keitel, Phys. Rev. Lett. **91**, 173202 (2003).

[52] P. Emma *et al.*, Nature Photon. **4**, 641 (2010).

[53] ANDOR technology, *X-ray cameras* [http://www.andor.com/scientific_cameras/xray/] (2010).

[54] R. L. Sandberg *et al.*, Phys. Rev. Lett. **99**, 098103 (2007).